CrossMark

The Observation of Plasmonic Talbot Effect at Non-Illumination Side of Groove Arrays

Mehdi Afshari-Bavil [1,2] · Xiaoping Luo [1,2] · Chuanbo Li [3] · Shuai Feng [3] · Mingli Dong [1,2] · Lianqing Zhu [1,2]

Abstract

Talbot effect in a metallic groove array is observed numerically based on finite element method (FEM) and verified theoretically based on non-paraxial approximation. Grooves in the metallic layer are separated from backside with a narrow gap that is smaller than surface plasmon (SP) penetration depth in metal. At certain circumstances, SPs tunnel through the gap and constructively interfere beneath the metallic layer. In propagation pattern, called Talbot carpet, self-images at certain distances in a periodic row parallel the metallic layer are formed. The distance, called Talbot distance, is coincident with non-paraxial approximation result. To evaluate the periodicity of revivals, new parameters such as R-square, contrast, and image size are introduced. Afterwards, influence of the structural parameters such as groove size, period, and gap thickness on the light intensity is analyzed and proper values for near-infrared wavelength range is determined. We anticipate that our finding reveals better understanding of SP tunneling and paves a way toward utilization of this effect in Talbot effect attributed applications, particularly image processing.

Introduction

Due to near-field diffraction [1], apertures satisfying $d^2 >> L\lambda$ where d, L, and λ represent aperture width, observation distance, and wavelength, respectively, show a unique effect that is discovered by H. F Talbot in 1836 [2] and thereafter recognized as Talbot effect. In this effect, self-images appear after transmission or reflection from a finite or infinite periodic array. Rayleigh [3] used Fresnel diffraction integral and derived an analytical relationship to determine the location of self-images. The effect is widely utilized in various optical applications such as interferometric measurements [4] lithography [5], microlens [6], array illumination [7], and trapping [8].

Because Talbot effect is a wave optics phenomenon, it is expected to be observed in all kinds of optical waves including SPs [9]. SPs are under-diffraction electromagnetic waves that propagate at the interface between metal and dielectric and attracted great attention in light manipulation [10–15]. Due to wave nature of SPs, researchers were motivated to explore plasmonic Talbot effect as well [16–23]. Among them, Chowdhury et al. for the first time discovered self-imaging through periodic nanohole arrays by using scanning aperture microscopy [20]. Later, Maradudin et al. investigated a periodic row of circular metallic dots and proved that transmitted SPs exhibit Talbot effects as well [24]. It has been demonstrated that plasmonics Talbot image is observable for the wavelengths smaller than the array period [16]. Meanwhile, the Talbot distance, in plasmonics regime was not coincident with the paraxial approximation, and modified formula was introduced to explain this deviation by Oosten et al. [25]. However, some research gap on plasmonic Talbot effect is still existing, especially those related to exploring this effect in complicated structures and exploiting the effect in numerous applications.

This paper adopts FEM-based numerical approach to demonstrate plasmonic Talbot effect behind the metallic layer while there is no slits or holes drilled on it. Albeit it should be noted that the separation between bottoms of grooves and

✉ Mehdi Afshari-Bavil
mehdi.afshari@bistu.edu.cn

1   Joint International Research Laboratory of Advanced Photonics and Electronics, Beijing Information Science and Technology University, Beijing 100192, China

2   Beijing Key Laboratory for Optoelectronic Measurement Technology, Beijing Information Science and Technology University, Beijing 100192, China

3   School of Science, Minzu University of China, Beijing 100081, China

the back surface should be considered accurately to assist SP tunneling to the backside of the metallic layer through the gap. Our results are determined by introducing new physical parameters such as R-square, an estimation of wave periodicity, size, and contrast.

Structures Description and Simulation Setup

Our schematic structure predicted in Fig. 1 consisting an infinite periodic groove array drilled on a silver film with period P, groove width W, and film thickness H. The incident light is z-polarized beam with the intensity normalized to unit. In the simulations, the permittivity of the silver (ε_m) is described by Drude model ($\varepsilon_m = \varepsilon_\infty - \omega_p^2/(\omega^2 + i\omega\gamma)$) which is coincident with experimental data in near-infrared range. The high-frequency bulk permittivity, ε_∞; the bulk plasmon frequency, ω_p; and the electron collision frequency, γ are 4.2, 1.346×10^{16}, and 9.617×10^{13} rad/s, respectively [26]. Meanwhile $\omega = 2\pi c/\lambda_0$ where c and λ_0 stands for light speed and incident wavelength is fixed to 632.8 nm. Numerical analysis is carried out through COMSOL that is a FEM algorithm-based commercial software. Due to symmetry, structure simplified as two-dimensional geometry with nine periods. The mesh size inside the grooves and narrow gap is considered 5 nm while in the rest of area, it is 20 nm to drastically reduce the simulation time and thereby the amount of information store to memory. Scattering boundary condition was applied for top and bottom boundaries, whereas periodic boundary condition was applied for side boundaries. The geometrical parameters are set to be H, 150 nm; h, 20 nm; P, 1220 nm; and α, 0.5 that gives $W = d = 610$ nm, The gap (h) is a critical parameter and plays significant role in either preventing or permitting SP tunneling through it. To characterize the appropriate groove width and period, this research adopted the approach of Zhang et al. [27] and introduced an "opening" ratio, α, defined as; $\alpha = d/P$ which has a range between 0 and 1. Unlike periodic hole array that periodicity should take specific values to overcomes the mismatch between impinging light and SPs wave vectors and excite SPs at the illumination side, the groove array is a broadband device in visible range.
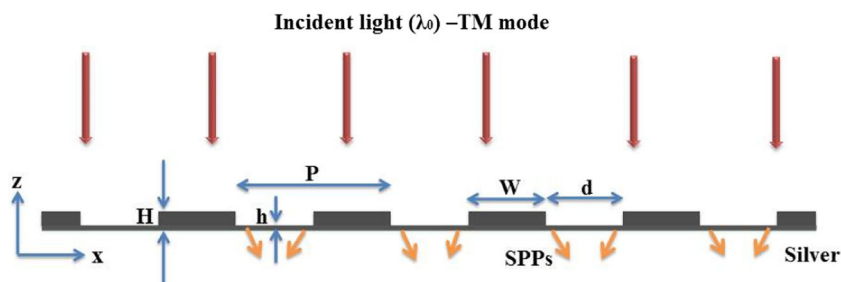
Results and Discussion

SPs excite at the illumination surface, propagate toward the grooves, penetrate through the gap, and finally propagate to free space beneath the metallic layer. The penetration depth is expressed by [9] $\lambda_0/(2\pi\sqrt{|\varepsilon_m|})$. The penetration depth plays a fundamental role, and must be considered carefully. For our working wavelength that is considered between 550 and 750 nm, the penetration depth is between 23 and 30 nm. This approves that our selected gap thickness is appropriate to allow SPs tunnel through the gap and propagate under the metallic layer. Due to short propagation length, the SP intensity propagating under the metallic layer decays rapidly when move away from interface. The propagation length is expressed by $L_{sp} = 1/\text{Im}(2k_{sp})$, where $k_{sp} = 2\pi/\lambda_{sp}$ and $\lambda_{sp} = \lambda_0\sqrt{((\varepsilon_{m+1})/\varepsilon_m)}$ which is strongly wavelength dependent [9] and for our working wavelength range, it differs from 8 to 85 μm. The light intensity under the metallic layer compared to nanoholes and nanoslits is lower; however, Talbot self-images are still observable. When the light illuminate the structure, the SPs are excited and assist in light transmission and from Talbot images in magnetic field spectrums as depicted in Fig. 2. For the sake of higher visibility, the spectrums are shown in logarithmic scale.

Furthermore, it is worthy to note that the green spots in Talbot carpets correspond with the shadow points in real picture. The Talbot revivals (self-images) are created in distances called Talbot distance τ, whereas another image, called fractional revivals, is formed at $\tau/2$. Lines A and B are corresponding to non-paraxial and paraxial ($P/\lambda \gg 1$) estimation of Talbot distances, respectively. The theoretical derivation of paraxial [3] ($\tau = 2P^2/\lambda$) and non-paraxial regime can be found somewhere else [25]. However, line A is placed in close proximity to the center of spots that verifies non-paraxial approximation is valid for plasmonics groove arrays. In non-paraxial approximation, the Talbot distance is expressed by [25]:

$$\tau = \lambda_{SP}/\left\{1-\left[1-(\lambda_{SP}/P)^2\right]^{1/2}\right\} \tag{1}$$

The first Talbot revival is located at 4.36 μm. Higher orders of Talbot revivals are formed at $n\tau$ where n is an integer number starting from 2. The propagation length for this wavelength is

Fig. 1 Schematic 2D sketch of the proposed groove array structure. Geometrical parameters are indicated in the picture

Fig. 2 Talbot images are created under the metallic layer in magnetic field spectrum. Lines A and B stand for paraxial and non-paraxial Talbot distance location
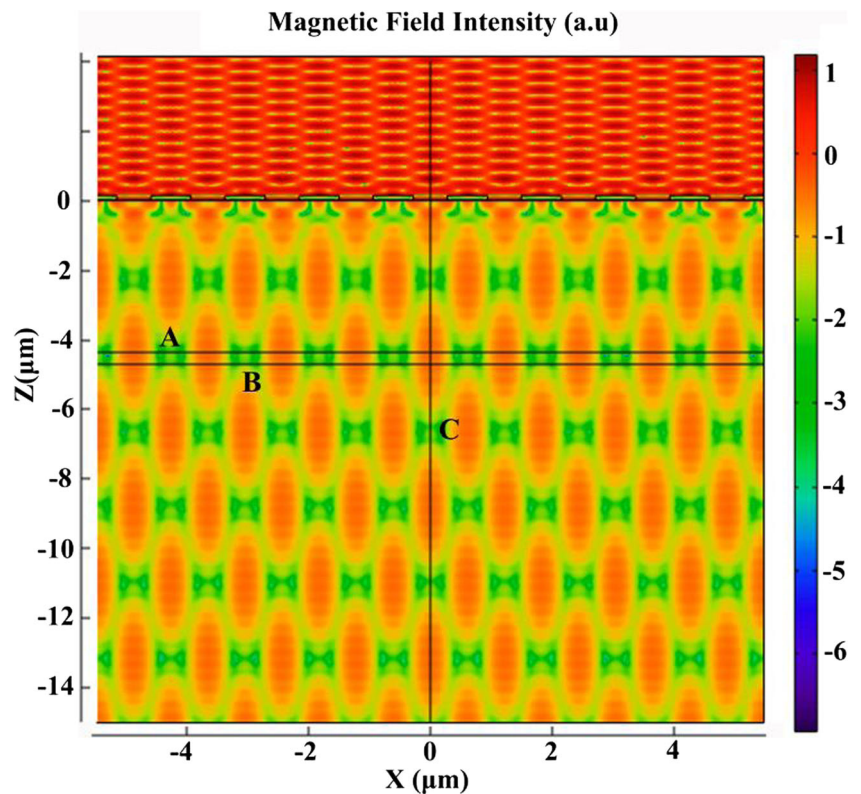
36 μm indicating that at least eight orders of revivals can be formed without any significant loss in light intensity. Practically, the propagation lengths can be dramatically improved by considering higher wavelengths. Figure 3a shows the light intensity along the line C located at the center of a groove. First and higher orders of Talbot revivals, Talbot distance, periodicity of Talbot carpet, and full width in half

maxim (FWHM) are benchmarked on the curve. FWHM is about 3.36 μm, which is bigger than half of the Talbot distance. The wavy nature on the curves might be attributed to diffraction effect. R-square is a criterion of wave deviation from an ideal periodic function. It is a direct output result in fitting tool box in MATLAB, when Fourier fitting type is utilized. R-square of the intensity profile along line C is

Fig. 3 Light intensity along line C (a) and A (b). E_{max}, E_{min}, and revival size are presented on the curves
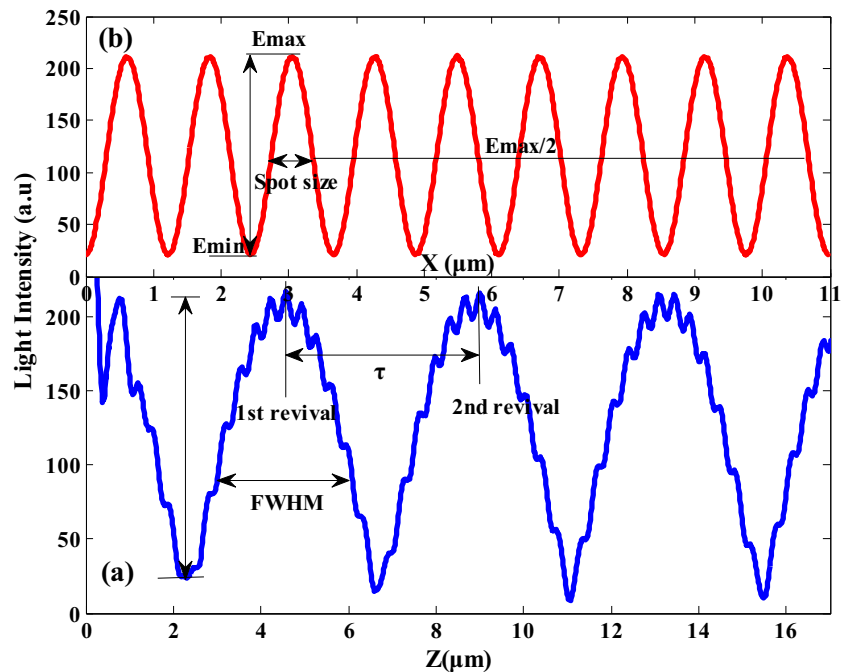
obtained 95%. The more the curve is coincident with the periodic behavior, the better the Talbot carpet is (in the ideal case where there is no fluctuation, R-square is 100%).

Two other parameters to describe revivals' quality are the size (along x direction at the first revival) and the contrast. (1) Size is calculated according to the following method: the peak intensity and the minimum intensity of the valley adjacent to the peak along x direction at the Talbot distance are drawn. Then, middle intensity between peak and minimum intensity is drawn as shown in Fig. 3b, the width cut out by this line on the intensity contour gives the revival size which is 750 nm, bigger than actual groove width. The closer the size to actual groove size is, the better the revival is. (2) Contrast is defined as the difference between peak and minimum on light intensity contour along the Z direction over the peak value multiplied by 100 that is obtained 90.68%. Since the light intensity is entirely space-dependent, the contrast is considered for the first revival. For an ideal Talbot carpet, the FWHM should be small, but the contrast and the R-square should be large. The gap is a critical parameter that can either block or permit SP tunneling. Figure 4 shows how light intensity changes with increasing the gap; however, the Talbot distance does not change. From Fig. 4a, it can be seen even though the curves have different intensities the shape of curves including the wideness and fluctuations does not change resulting in identical R-square and FWHM. It was expected that the gap only affects the amount of SP tunneling. The contrast variation is shown in the left inset of Fig. 4 in which $h = 15$ nm has the best performance. But the light intensity drops rapidly which is shown in the right inset of Fig. 4. The intensity is normalized with the maximum intensity which is related to $h =$

5 nm in our simulation data. The light intensity variation along the line A located on Talbot distance is represented in Fig. 5. Light intensity dropped sharply, while the revival size is enhanced smoothly as shown in the inset of Fig. 5. Our results show that better images are achieved when the gap is narrow; however, it is impractical to fabricate such deep grooves. It seems that h between 15 and 20 nm has good compromise between fabrication limits and intensity loss. Moreover, we realized for silver thickness within the range of 50~300 nm, the film thickness variation does not have considerable effect on Talbot contour, demonstrating that any film thickness within this range produces similar Talbot contour. In our work, the film thickness is fixed at 150 nm.

Discussion on Geometrical Parameters

The "opening" ratio $\alpha = d/P$ is another parameter that should be investigated in more details. However, it is correlated to another parameter: $\gamma = P/\lambda$. Previously, Hua et al. demonstrated the criteria of γ for nanohole array [28]. In similar way, we can obtain an effective working range for groove array. Three different situations can be imagined:

(a) P, λ: fixed, α: variable

Here, we considered a fixed wavelength and period while α is variable. Variation on α was achieved by changing d to tune the groove and step thicknesses. We fixed P and λ values as before and altered α from 0.2 to 0.7. We

Fig. 4 Light intensity versus gap thickness. (b) Contrast and (c) Normalized peak intensity versus gap thickness
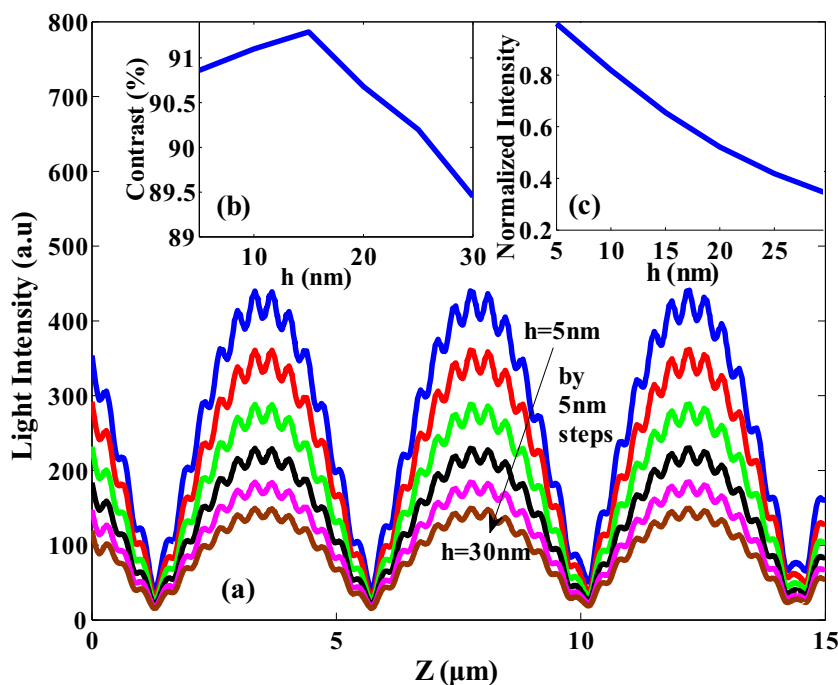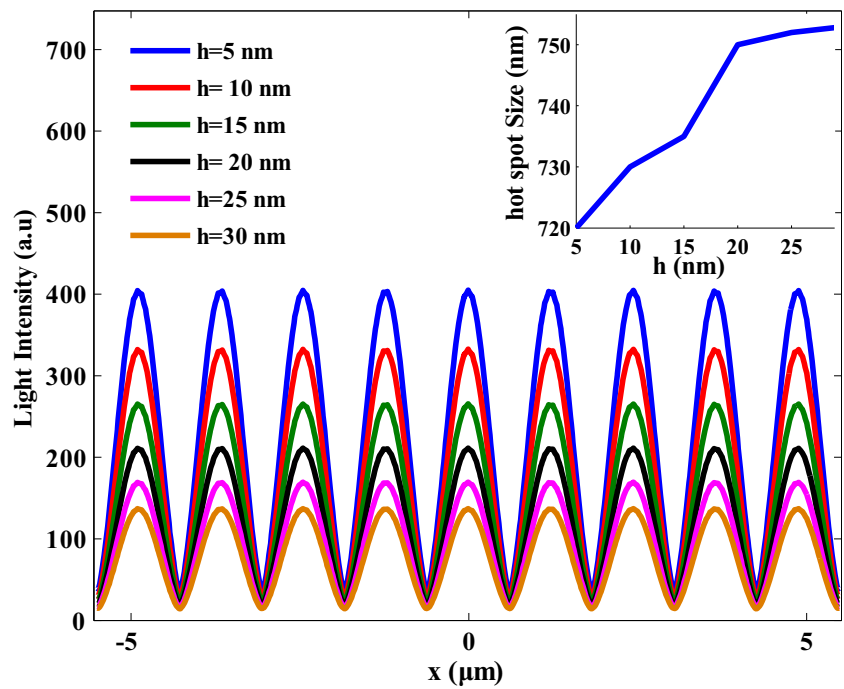
Fig. 5 Light intensity variation along x direction at Talbot distance for different gap thicknesses. Inset shows revival size variation with gap thicknesses

In this situation, we set wavelength as before and let the period to be swept for wide range from $P = \lambda$ to $P = 3\ \lambda$. Ideally, it is required that for each P, the simulation run to find the best value of α. However, for the purpose of avoiding protracted simulation time and thereby saving memory, we randomly selected some periods and swept α to find the best working range. We observed that, for each period, the optimized value of α was still within the range of 0.5 to 0.58 as indicated in Fig. 7. Consequently, we fixed the value of α as 0.54 for the entire period range. For the R-square less than 90%, the Talbot image is damaged, so we considered γs that their R-square is greater than 90%. Three different regimes are recognized:

$\gamma \leq 1.25$ and ≥ 2: Talbot image was not formed.

ignored both higher and lower values of α because the fact that such values result in ultra-thin slits and ultra-thin steps; that is impractical from fabrication point of view. The results are shown in Figs. 6 and 7.
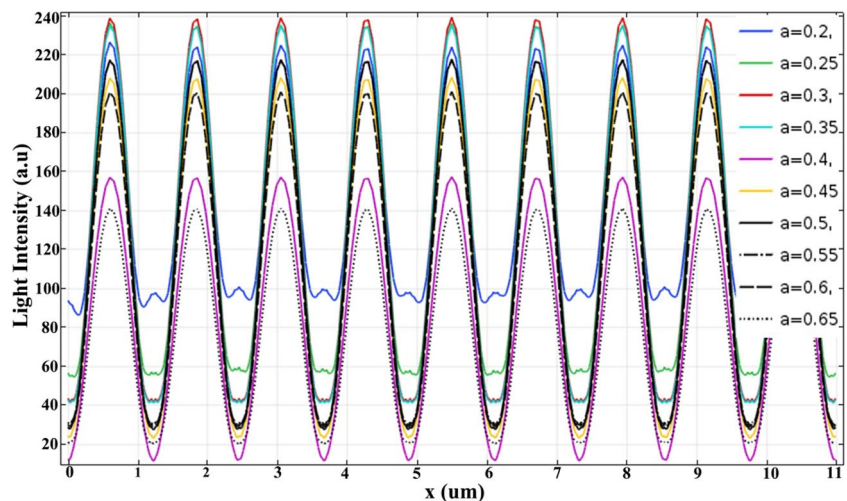
At higher values of α, intensity and R-square drop very steadily. At smaller α value, despite larger intensity, minima happens at considerably high intensities, which make the spots unclear with smaller R-square values. From Fig. 7, it can be seen that for α located between 0.5 and 0.58, R-square is nearly constant and stable, where we call it "working range." Due to inaccuracy during fabrications, introducing range instead of values for α can decrease the fabrication obstacles.

(b) λ: fixed, P: variable

Fig. 6 Light intensity variation along Talbot distance for various opening ratios
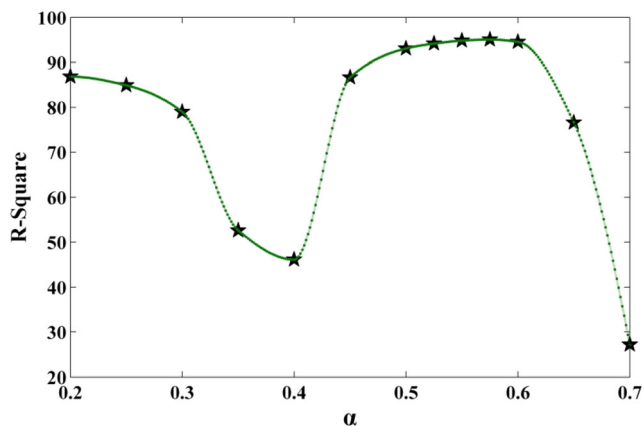
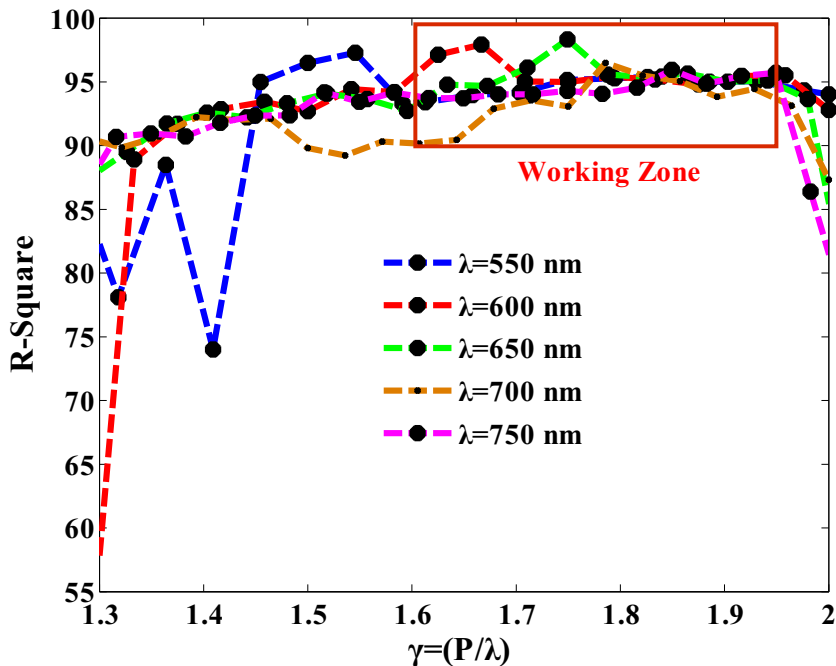**Fig. 7** R-square versus opening ratios

$1.25 < \gamma < 1.7$, $1.95 < \gamma < 2$: Talbot image was formed but R-square is less than 90% or Talbot distance does not fit with non-paraxial predictions.

$1.7 < \gamma < 1.95$: Talbot image was formed and agrees quite well with non-paraxial predictions. We name the third regime as the working zone.

(c) λ and P: variable

In this case, we still fix α at 0.54. For each wavelength, in certain periods, Talbot revivals are formed. We considered some wavelengths within visible range, similar to situation (b), for each wavelength three regimes are introduced, for $\gamma \leq 1.25$ and ≥ 2, our results showed Talbot image does not appear again. However, for the range between these values, Talbot image created and we achieved similar result as part (b), but the working zone is within 1.63 to 1.95 as shown in Fig. 8. To generalize our result, by mixing the working range

of unit b and c, the suitable working zone for any wavelength within visible range is determined between 1.7 and 1.95. Simply speaking, for each wavelength appropriate period and groove width could be simply derived through their working zone values.
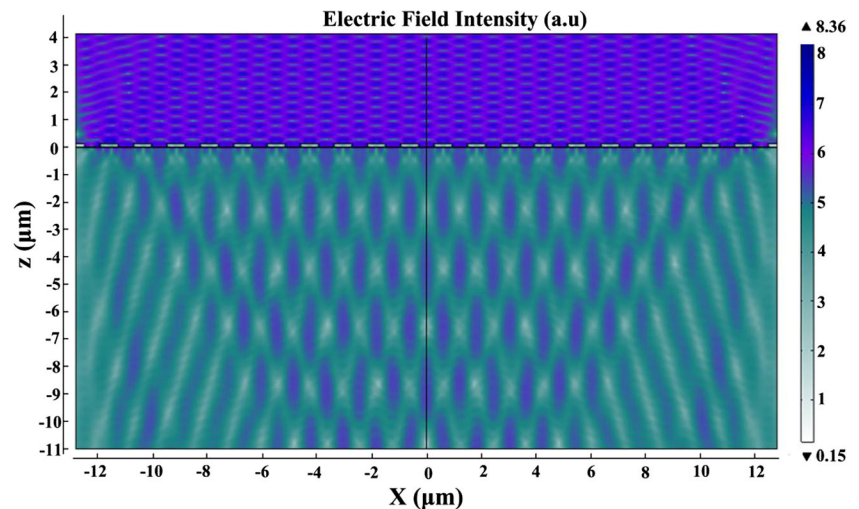
Furthermore, when we considered very longer periods, it was found that for $\gamma > 5$, some revivals appeared but the Talbot carpet was not clear. However, by considering a maximum value for revivals, their location was obtained in coincidence with paraxial Talbot distance. It should be noted that at large periods both paraxial and non-paraxial approaches give identical results.

Finally, it was found, if finite groove array is replaced by infinite array, 13 grooves are needed to observe the first revival. In addition, to have two successive revivals raw, 19 grooves are needed. Figure 9 shows a finite array with 21 grooves, at higher revivals; due to boundaries, only self-images located at the central area are formed, which confirms the focusing nature of groove array that will be studied in our future work on nanofocusing.

Summary

In conclusion, we have observed Talbot effect in a metallic groove arrays by adopting FEM method. For gaps with thickness less than penetration depth, SPs tunneled through the gap and under the metallic layer, and due to interference, create Talbot revivals. The Talbot distances can be determined through non-paraxial formula. FWHM, R-square, size, and contrast are introduced and calculated.

Fig. 8 R-square versus γ for different wavelengths. The rectangle represents the working zone

Fig. 9 Talbot image of finite groove array with 21 grooves

Influence of geometrical parameters variation on formation of Talbot images was analyzed. We introduced two applicable opening ratio parameters at three different regimes. For near-infrared wavelength range, the opening ratio should be considered between 0.5 and 0.58. Meantime, period to wavelength should be considered within 1.7 and 1.95. Our results can offer an improved understanding of SPs nature. It will also offer additional advantages of groove array-based structures for a wide range of applications including high-resolution imaging, Talbot image-assisted applications and nanolithography.

References

1. Fresnel A (1819) Mémoire sur la diffraction de la lumière. Da P 339 a P 475 1 Tav Ft AQ 210:339
2. Talbot HF (1836) LXXVI. Facts relating to optical science. No. IV. London Edinburgh Philos Mag J Sci 9:401–407
3. Rayleigh L (1881) XXV. On copying diffraction-gratings, and on some phenomena connected therewith. London, Edinburgh, Dublin Philos Mag J Sci 11:196–205
4. Liu L (1989) Talbot and Lau effects on incident beams of arbitrary wavefront, and their use. Appl Opt 28:4668–4678
5. Stuerzebecher L, Harzendorf T, Vogler U, Zeitner UD, Voelkel R (2010) Advanced mask aligner lithography: fabrication of periodic patterns using pinhole array mask and Talbot effect. Opt Express 18:19485–19494
6. Gao H, Hyun JK, Lee MH, Yang JC, Lauhon LJ, Odom TW (2010) Broadband plasmonic microlenses based on patches of nanoholes. Nano Lett 10:4111–4116
7. Maddaloni P, Paturzo M, Ferraro P, Malara P, De Natale P, Gioffrè M et al (2009) Mid-infrared tunable two-dimensional Talbot array illuminator. Appl Phys Lett 94:121105
8. Song YG, Han BM, Chang S (2001) Force of surface plasmon-coupled evanescent fields on Mie particles. Opt Commun 198:7–19
9. Maier SA (2007) Plasmonics: fundamentals and applications. In: Springer Science & Business Media
10. Bavil MA, Liu Z, Zhou WW, Li CB, Cheng BW (2017) Photocurrent enhancement in Si-Ge photodetectors by utilizing surface plasmons. Plasmonics 12:1709–1715
11. Bavil MA, Deng Q, Zhou Z (2014) Extraordinary transmission through gain-assisted silicon-based nanohole arrays in telecommunication regimes. Opt Lett 39:4506–4509
12. Zhi GA, Jin HS, He C, Guo FS, Jia KS, Yu YS et al (2016) Nanoplasmonic-gold-cylinder-array-enhanced terahertz source. J Semicond 37:123002
13. Hess O, Pendry JB, Maier SA, Oulton RF, Hamm JM, Tsakmakidis KL (2012) Active nanoplasmonic metamaterials. Nat Mater 11:573–584
14. Wang J, Yang G, Zhang Q, Gao S, Zhang R, Zheng Y (2017) Localized surface plasmon-enhanced deep-UV light-emitting diodes with Al/Al2O3 asymmetrical nanoparticles. Plasmonics 12:843–848
15. Wang J, Yang G, Ye X, Zhang Q, Gao S, Chen G (2017) Tailoring the multiple Fano resonances in nanobelt plasmonic cluster. Plasmonics 12:1641–1647
16. Li W, Li H, Gao B, Yu Y (2017) Investigation on the plasmon Talbot effect of finite-sized periodic arrays of metallic nanoapertures. Sci Rep 7:45573
17. Shi XY, Yang W, Xing H, Chen X (2015) Discrete plasmonic Talbot effect in finite metal waveguide arrays. Opt Lett 40:1635–1638
18. Wang Y, Zhou K, Zhang X, Yang K, Wang Y, Song Y, Liu S (2010) Discrete plasmonic Talbot effect in subwavelength metal waveguide arrays. Opt Lett 35:685–687
19. Cherukulappurath S, Heinis D, Cesario J, van Hulst NF, Enoch S, Quidant R (2009) Local observation of plasmon focusing in Talbot carpets. Opt Express 17:23772–23784
20. Chowdhury MH, Catchmark JM, Lakowicz JR (2007) Imaging three-dimensional light propagation through periodic nanohole arrays using scanning aperture microscopy. Appl Phys Lett 91:1–4
21. Dennis MR, Zheludev NI, García de Abajo FJ (2007) The plasmon Talbot effect. Opt Express 15:9692–9700
22. Iwanow R, May-Arrioja DA, Christodoulides DN, Stegeman GI, Min Y, Sohler W (2005) Discrete Talbot effect in waveguide arrays. Phys Rev Lett 95:1–4

23. Zhao WS, Eldaiki OM, Yang RX, Lu ZL (2010) Deep subwavelength waveguiding and focusing based on designer surface plasmons. Opt Express 18(20):21498–21503

24. Maradudin AA, Leskova TA (2009) The Talbot effect for a surface plasmon polariton. New J Phys 11:33004

25. Van Oosten D, Spasenović M, Kuipers L (2010) Nanohole chains for directional and localized surface plasmon excitation. Nano Lett 10:286–290

26. Palik ED (1998) Handbook of optical constants of solids, vol 3. Academic press, Cambridge

27. Zhang W, Zhao C, Wang J, Zhang J (2009) An experimental study of the plasmonic Talbot effect. Opt Express 17:19757–19762

28. Hua Y, Suh JY, Zhou W, Huntington MD, Odom TW (2012) Talbot effect beyond the paraxial limit at optical frequencies. Opt Express 20:14284–14291